scientific reports

Check for updates

OPEN

Improvement of anti-corrosion performance of an epoxy coating using hybrid UiO-66-NH$_2$/carbon nanotubes nanocomposite

Jafar Abdi[1], Mazdak Izadi[2] & Mansoor Bozorg[1]✉

In this study, a porous nanocontainer from UiO-66-NH$_2$/CNTs nanocomposite with an excellent barrier characteristics was constructed through amine-functionalized Zr-based metal organic framework. The characterization of the prepared nano-materials were performed using different analyses such as FTIR, XRD, SEM, EDS, TEM, and BET and the results proved the successful synthesize of UiO-66-NH$_2$/CNTs nanocomposite. The corrosion protection performance of the coated panels was investigated by electrochemical impedance spectroscopy (EIS), salt spray, and contact angle measurement. The EIS results revealed that unmodified and UiO-66-NH$_2$ containing coating in 3.5 wt.% NaCl electrolyte were failed after 45 days but the corrosion was negligible in UiO-66-NH$_2$/CNTs coating due to high pore resistance values even after 45 days. Salt spray and contact angle measurements confirmed that UiO-66-NH$_2$/CNTs containing coating acts as an efficient barrier against wet saline environment even at long exposure times. This is attributed to uniform dispersion in the epoxy matrix and formation of a uniform nanocomposite coating.

As a promising material for delaying ions and water molecules from reaching to metals' surface, polymeric coatings act like a physical barrier. The epoxy resins could be considered as a group of distinguished thermosetting polymers with outstanding features of excellent resistance to moisture, remarkable resistance to solvents, excellent mechanical and thermal properties, and great adhesion properties to various surfaces of both metals and non-metals. Due to its excellent properties, this material has been utilized in a wide range of industries including aircraft construction, car industries, and petroleum industries; Nevertheless, suffering from some salient weaknesses such as poor crack deflection performance, and brittleness, it couldn't be used in many applications[1,2]. Therefore, finding a suitable alternative for epoxy resin among organic coatings is challenging as these materials are not water-proof and totally perfect. Resultantly, in a corrosive environment, metals could not be preserved for long period. Formation of defects (in micro-scales) in the structure of coatings is almost inevitable. The situation gets worse when the material is designed for outdoor application where it experiences harsh and uncontrolled conditions. Bypassing the coating material, the structural defects result in the corrosion of metal. So as to prevent such a kind of problem, a new generation of coating with the ability of anti-corrosion has been constructed. The protective ability could be improved by addition of nano/micro additives to the structure of epoxy-based coatings. Various investigations have dealt with the construction of high quality nanocomposites with excellent mechanical and thermal features[3–5]. A wide variety of nanofillers are investigated and chosen for enhancement of the coatings' protectiveness. For example some of carbon-based nanofillers are: carbon nanotubes[6,7], graphene and graphene oxide[8,9], inorganic nanomaterials such as LDH[10], fullerene[11], and halloysite[12] and clay[13], etc.

In recent decades, a group of porous materials with a 3D structure have been widely investigated and developed significantly. Since introduced as materials with nanopore structure, modifiable properties by replacing its ligands, and astonishingly large surface areas, metal–organic frameworks (MOFs) have attracted many attentions[14–19]. Additionally, these porous materials have been contemplated as promising candidates for fabrication of anti-corrosion coatings with barrier capability. Furthermore, not only the resulted coatings will prevent corrosion properly, but also it has been observed that they are relatively impermeable. Unfortunately, rarely reports could be found covering the application of MOFs in the fabrication of anti-corrosion coatings or their application as a protective layer[20–31]. In this regard, there are some works that introduce bare MOFs imparted

[1]Faculty of Chemical and Materials Engineering, Shahrood University of Technology, Shahrood 3619995161, Iran. [2]Department of Materials Engineering, Hamedan University of Technology, Hamedan 6516913733, Iran. ✉email: m.bozorg@shahroodut.ac.ir

with corrosion resistance without the need of any post-synthetic modifications. Roy et al.[32] synthesized a three dimensional supramolecular porous framework Zn(OPE-C$_{18}$)0.2H$_2$O (NMOF-1) with high water contact angles and corrosion resistance. In other study, Zhang et al.[27] took an initiative to investigate the potential application of ZIF-8, one of the most widely studied hydrophobic and water stable MOFs, in the anticorrosion industry. Etaiw et al.[23] obtained brown crystals of the MOF (AgCN)$_4$(qox)$_2$, and employed it as corrosion inhibitor for C-steel in 1 M HCl solution. Recently, Fouda et al.[33] prepared silver based MOFs as corrosion inhibitors in acid environment and Kumaraguru et al.[29] reported the preparation of nickel, copper, and cobalt MOFs employing the corresponding metal salts and trimesic acid as ligand and their anticorrosion properties.

Although, MOFs are extremely porous (typically have a void space of more than 40%), practical, and appropriate for many applications. The mechanical properties of the developed MOFs are yet to be understood in details. Having a plethora of outstanding features like low density, remarkable surface area, and modifiable porous structure, MOFs have been integrated into various fields. Among them, adsorption[34–37], catalysis[38–42], and photocatalysis[43–47], could be mentioned. Therefore, the sophisticated composite materials could be fabricated using MOFs and their unique mechanical and thermal properties[48,49] and anti-corrosion features[50,51]. Ma et al.[52] added Sn-MOF@PANI and observed that the mechanical and thermal characteristics of the investigated epoxy composite coatings improved. Similarly, Zhang et al.[53] showed that the epoxy coating's resistance to fire was significantly intensified as a result of hybridization between MOFs and GO nanosheets.

In recent years, the thermal stability, high strength when exposed to shear forces, nanosize structure, and notable surface area of zirconium-based MOFs has caught the researcher's imagination especially for some applications like separation of various components and drug delivery[54–59]. In recent investigations, zirconium-based MOFs have been paid attention due to their high elasticity module (G)/ shear modulus (more than 13 GPa) in comparison to the other MOFs. For example, it has been found that Zr-based MOFs generally have a shear modulus value about 5–10 times of other well-known MOFs like ZIF-8. Additionally, Zr-based MOFs have a mechanically, chemically, and thermally stable structures due to numerous organic–inorganic nodes between Zr atoms and 2-ATA. Having a perfect coordination between organic and inorganic parts, the zirconium-based MOFs benefit from outstanding mechanical features and a stable structure when experiencing a shear stress[57]. Sai et al.[60] examined the effect of Zr$_6$O$_4$(OH)$_4$ clusters and 1,4-benzodicarboxylic acid, as the metal node and organic ligands, respectively, on the thermal stability of the synthetized MOF in fire. Likewise, Guo et al.[49] conducted research on covering CNTs with SiO$_2$@UiO-66 particles and it was found that their resistance against flames improved significantly and the epoxy coating successfully acted like an organic–inorganic inhibitor against the corrosion issue. In order to protect metals against corrosion, scientists have synthesized new CNTs-based coatings known as the superhydrophobic coatings (SHCs)[61]. It is noteworthy to mention that the limited interactions between polymer chains and the CNTs used in the structure of epoxy and the low dispersion of CNTs in the matrix of epoxy coatings are challenging. Therefore, it is of utmost importance to control the CNTs entanglement and the uniform dispersion of them in the final coating. Surface modification of CNTs is a convenient way to reduce the interaction of nanotubes. A plethora of approaches just have focused on the enhancement of the oxygen/water/ion preventing properties of high-performance coatings which are filled with upgraded CNTs in the form of nanocomposite additive.

Considering the above concerns, composites based on the UiO-66-NH$_2$ and CNTs can provide the anti-corrosion properties. Some UiO-66-NH$_2$/CNTs composites have been synthesized for various applications such as fabricating transistors[62], dye separation[63], electrocatalytic sensing[64,65], and photocatalytic CO$_2$ reduction[66]. To the best of our knowledge, the report regarding decorating the UiO-66-NH$_2$ with CNTs yet to be investigated. In the presented study, aiming for addressing the mentioned gap in the literature, authors have fabricated a UiO-66-NH$_2$/CNTs nanocomposite for enabling the epoxy coating to act as an anti-corrosion coating. So as to accomplish these goals, a Zr-based MOF functionalized by amine group was employed. The properties of the developed MOF/CNTs were analyzed by various methods, such as FTIR, XRD, SEM, EDS, TEM and BET. Afterwards, electrochemical impedance spectroscopy (EIS) tests, salt spray and contact angle measurement were applied on CNTs, UiO-66-NH$_2$, and UiO-66-NH$_2$/CNTs incorporated epoxy composites to analyze their performance in their anti-corrosion characteristics.

Experimental

Materials. Zirconium tetrachloride (ZrCl$_4$, 98%) and 2-Aminoterephthalic acid (ATA, 99%) were used as metal and organic precursors of MOF, respectively bought from Sigma-Aldrich. Utilized solvents including methanol, N, N-dimethylformamide (DMF, 99%), nitric acid (HNO$_3$, 68%), sulfuric acid (H$_2$SO$_4$, 98%) and acetic acid (HAc, 98%) were provided by Merck company. Carbon nanotubes were purchased from Plasma-Chem GmbH and used without further purification. Epoxy resin (Araldite GZ7 7071X75: solid content: 74–76%, epoxy value: 0.15–0.17, density: 1.08 g/cm³) was purchased from Saman Co. Furthermore, amido polyamide curing agent based on CRAYAMID 115 (Arkema Co.) was employed as curing agent. In this research work, mild steel (CK10) was used as substrate. The chemical composition (wt.%) of the steel was as follows: 0.1 wt.% C, 0.45 wt.% Mn, ma×0.4 wt.% Si, and about 99 wt.% Fe. Steel panels were cut into the size of 30×20×1 mm and 80×50×1 mm. Then the surface was polished with SiC paper of graded grit sizes ranging from 120 to 1500 to achieve a mirror-shinning surface then ultrasonically cleaned in a mixture of acetone and ethanol for 10 min. Finally samples were washed with distilled water and then dried in air.

Preparation of UiO-66-NH$_2$. Primarily, zirconium tetrachloride (0.095 g) and amino-functionalized ligand, NH$_2$-BDC (0.067 g) were separately dissolved in 15 mL of DMF solvent for 15 min using ultrasonic vibration. Next, the Zr^{4+} ions solution was mixed with the ligand solution containing 2 mL of acetic acid. Then, the final mixture was agitated for an hour, subsequently was moved into an autoclave (Teflon-lined stainless

steel) and was heated at 120 °C in the oven during 24 h. Finally, the mixture was cooled down, centrifuged and washed several times with methanol and dried at 70 °C to obtain UiO-66-NH$_2$ powder.

Preparation of UiO-66-NH$_2$/CNTs nanoparticles.   To prepare hybrid UiO-66-NH$_2$/CNTs nanocomposite, carbon nanotubes walls were primarily modified with negatively charged carboxyl groups (COOH$^-$). This act was performed by dispersing CNTs powder (1 g) into the mixture of sulfuric acid and nitric acid (100 mL) solution using ultrasonic instrument followed by refluxing at 80 °C overnight. Then, the functionalized CNTs were filtered and washed with deionized water until pH of 6 was achieved. After that, the filter cake was dried for 24 h at 70 °C for the subsequent procedure. Similar to the mentioned method for synthesizing UiO-66-NH$_2$ crystals, hybrid UiO-66-NH$_2$/CNTs nanocomposite was prepared. Therefore, modified CNTs were dispersed into the DMF solution (15 mL) containing zirconium chloride and 2-Aminoterephthalic acid ligand agitated for an hour. Then, the final mixtures was transferred into stainless steel autoclave and heated at 120 °C for 24 h. Finally, the mixture was cooled down, centrifuged and washed several times with methanol and dried at 70 °C to obtain UiO-66-NH$_2$/CNTs nanocomposite for further experimental tests. Fig. S1 shows a schematic of the synthesis process of UiO-66-NH$_2$@CNTs hybrid nanocomposite.

Preparation of CNTs, UiO-66-NH$_2$ and UiO-66-NH$_2$/CNTs epoxy nanocomposites.   To investigate the effect of synthesized composite material on the electrochemical behavior of epoxy coating, 0.5 wt.% of each materials were distributed in the epoxy resin and polyamide hardener mixture (at a ratio of 5/2 w/w) through an ultrasound-assisted procedure. The epoxy/polyamide mixture was diluted to reduce the viscosity. The epoxy coating with 0.5 wt.% of synthesized materials were applied on steel sheets by a film applicator. The coated samples were kept at 25 °C for 24 h and then cured at 80 °C for 1 h. The dry thickness of the coating was about 50 μm.

Characterization and techniques.   The fingerprint and structural functional groups of the materials were determined using Fourier transmitter infrared spectroscopy (FTIR, Perkin-Elmer, Spectrum One, USA). X-ray diffraction (XRD, PANalytical, Netherlands) was employed to distinguish crystal structure and the data was collected by Bruker D8 advance diffractometer utilizing Cu/Kα radiation source and voltage 40 kV, 40 mA, and 1.54056 Å. The sample was scanned between 5 and 65.95 degrees 2θ, in step sizes of 0.01° at a rate of 0.01° 2θ/second. The scanning electron microscopy (SEM) (LEO 1455VP, Oxford, UK) and transmission electron microscopy (TEM) (Zeiss-EM10C-100 kV, Germany) were run to find out the crystal size and the surface morphology of all samples. The specific surface area of the synthesized MOF and nanocomposite were identified using Brunauer–Emmett–Teller (BET) measurements (BELSORP-mini II, BEL, Osaka, Japan) by N$_2$ adsorption–desorption isotherm at 77 K.

Electrochemical impedance spectroscopy (EIS).   In order to study the electrochemical properties, a potentiostat/galvanostat (Autolab, PGSTAT 302 N) was used. Coated samples (1 cm^2 exposed area), saturated calomel electrode (SCE) and a platinum electrode were employed as working electrode (WE), counter electrode and reference electrode, respectively. Impedance measurements were performed by an AC signal with the amplitude of 20 mV peak to peak at the open circuit potential in the range of 100 kHz to 10 mHz frequency. The coated samples were immersed in 3.5% NaCl solution and EIS measurements were performed over time. The Nova (version 1.6) and Z-View2 softwares were used to data measurements and fit the EIS data via the electrical equivalent circuits (EEC), respectively. All EIS experiments were repeated for three times under the same conditions to ensure that the results are reproducible.

Salt spray test.   Salt spray exposure was carried out on the steel samples coated with epoxy coating. The test was done on the scratched samples for 500 h in salt spray cabinet according to ASTM B117. The NaCl concentration of salt fog was 5 wt.%. All samples were scratched with a dimension of 3 cm × 2 mm, created using a surgery knife.

Contact angle measurements.   Contact angles were measured using a home-made system at room temperature to investigate the static contact angles of distilled water droplet (5 μL) on the different coating. Water droplets were carefully placed onto the surfaces of the samples and the shape of droplet was recorded by canon digital camera. The homemade apparatus has been calibrate with standard references before measurements. The contact angle was determined from the average of five measurements at various positions on the samples surface.

Results and discussion

Characterization of the prepared materials.
Different characteristic analyses were investigated to confirm the successful preparation of the nanomaterials. The scanning electron microscopy (SEM) analysis was employed to evaluate the surface morphology and structural characteristics of the synthesized nanoparticles. Figure 1a shows the carbon nanotubes after acid-treatment, which possess about 10–35 nm diameter. Figure 1b illustrates the pure UiO-66-NH$_2$ crystals (50–400 nm) with a uniform and octahedral shape. The morphology of hybrid UiO-66-NH$_2$/CNTs nanocomposite reveals a three-dimensional interlinked network (Fig. 1c). It can be clearly seen that the CNTs and UiO-66-NH$_2$ nanoparticles retain their tubular and octahedral structures after hybridization. Also, EDS mapping represents the elemental scattering of C, O, N, and Zr in the UiO-66-NH$_2$/CNTs framework, verifying the successful fabrication of the nanocomposite. Further investigation was performed using transmission electron microscopy (TEM) analysis to show the micro-cavities of the nanoparticles
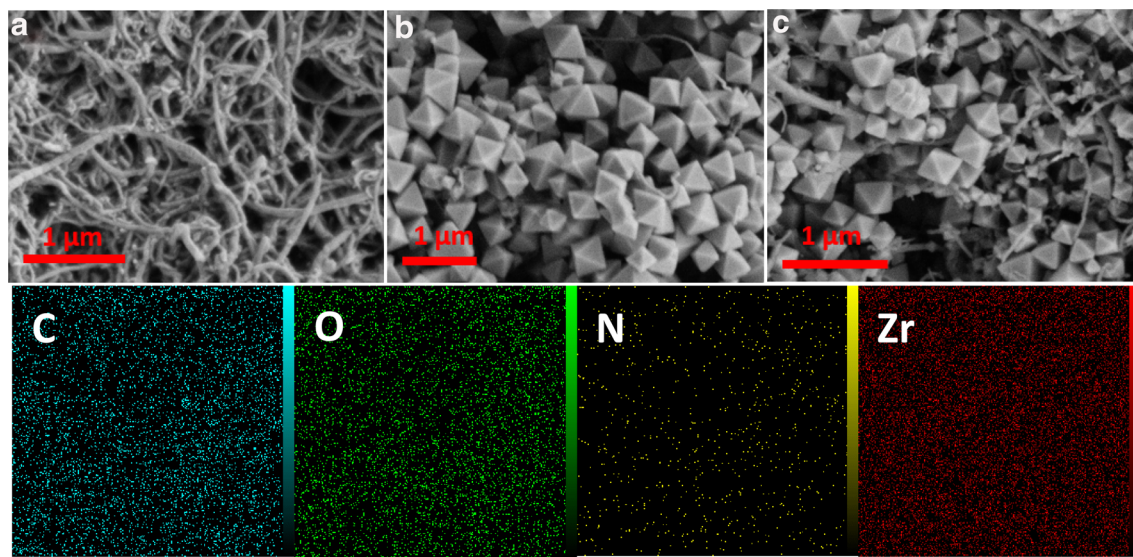
Figure 1. SEM images of (**a**) CNTs, (**b**) UiO-66-NH$_2$, (**c**) UiO-66-NH$_2$/CNTs, and EDS mapping of hybrid nanocomposite.

structure. Figure 2a shows the UiO-66-NH$_2$ particles, which confirms the octagonal structure with moderate aggregation. The TEM image of UiO-66-NH$_2$/CNTs hybrid nanocomposite with two different magnifications, shown in Fig. 2b, c, indicates the growth of UiO-66-NH$_2$ crystals on the outer wall of CNTs as clusters of grape. Also, the electron scattering pattern (Fig. 2d) for a selected area, clearly shows the bright spots in the form of a circular ring, which determines the frequency of the synthesized crystalline lattice structure. Electron diffraction is performed on a TEM by using the magnetic lenses of the beam column to focus the beam down to a point that can be aimed at a single particle or edge of a larger crystal. The result is a black image with points of light where the crystal structure is causing the beam to scatter. With the main beam blocked in the center of the image, these points of light or rings in the case of an amorphous or polycrystalline material can be used to calculate information on the crystal structure of the sample.

The FTIR spectra of CNTs, UiO-66-NH$_2$ and UiO-66-NH$_2$/CNTs hybrid nanocomposite are shown in Fig. 3a. The UiO-66-NH$_2$ spectrum illustrates three specific peaks (marked with small arrows) at 1400, 1580, and 1655 cm^{-1}. The FTIR peak at around 1400 cm^{-1} attributed to symmetric vibration of carboxyl group. The carbonyl group vibration band appeared at 1655 cm^{-1} and the peak at 1580 cm^{-1} ascribed to aromatic C=C stretching vibration. In addition, two typical peaks located at 788 and 1260 cm^{-1} attribute to N–H and C–N stretching band and confirm the presence of –NH$_2$ group in the UiO-66-NH$_2$ structure. Furthermore, two characteristic peaks at 3518 and 3337 cm^{-1} are derived from the asymmetric and symmetric vibrational bands of the primary amine group, respectively[67]. Some peaks existing in the range of 400–700 cm^{-1} are belonged to in-plane and out-of-plane –COO groups vibrations[68,69]. The FTIR spectra of UiO-66-NH$_2$/CNTs nanocomposite shows that the main bands are relatively remained with no variations in comparison with the pure UiO-66-NH$_2$. However, some small changes can be observed at some peaks such as 574 cm^{-1}, 1064 cm^{-1} (highlighted with orange color) and 1253 cm^{-1} (highlighted with green color), which is due to the interactions between CNTs and the MOF crystals (e.g. π–π interaction) and introducing functional groups brought with the acid-treated CNTs.

The phase structures of the prepared materials were further analyzed using XRD analysis for confirming the crystallinity. As shown in Fig. 3b, the characteristic peak with low intensity and a relative broad peak are observed at 23° and 43° in CNTs pattern which indicate amorphous crystal form and refer to (002) and (100) planes, respectively[70]. The XRD pattern of the UiO-66-NH$_2$ sample shows a great agreement with the patterns reported in literature (Fig. S2)[68,71]. The specific peaks appeared at 2θ = 7.3°, 8.5° and 25.6° attribute to the (110), (200), and (600) planes, respectively[65]. According to the XRD pattern obtained for the UiO-66-NH$_2$/CNTs nanocomposite, quite similar peaks to that of the UiO-66-NH$_2$ can be seen with no significant displacement, confirming that the UiO-66-NH$_2$ nanoparticles have been successfully loaded on the CNTs by employing the solvothermal preparation method.

N$_2$ adsorption–desorption isotherms of the nanomaterials were also investigated to measure the BET surface area, as shown in Fig. 3c. The obtained specific surface areas comprise 65.35, 1113, and 1064.4 m^2/g for CNTs, UiO-66-NH$_2$, and UiO-66-NH$_2$/CNTs, respectively (Table S1). All samples possess the type H$_3$ hysteresis loop and reveal type I isotherm according to the IUPAC suggesting microporous structure of the materials (Fig. S3). Additionally, the pore size distribution of different samples were shown in Fig. S4. The uniform pore structure confirmed that the samples had well-defined mesopores. Beside the SEM analysis, the elemental composition of the UiO-66-NH$_2$/CNTs sample was identified using energy dispersive spectroscopy (EDS) technique. Figure 3d represents the result of the EDS analysis which indicates the presence of carbon, zirconium, oxygen and nitrogen as the most dominant elements in the sample.
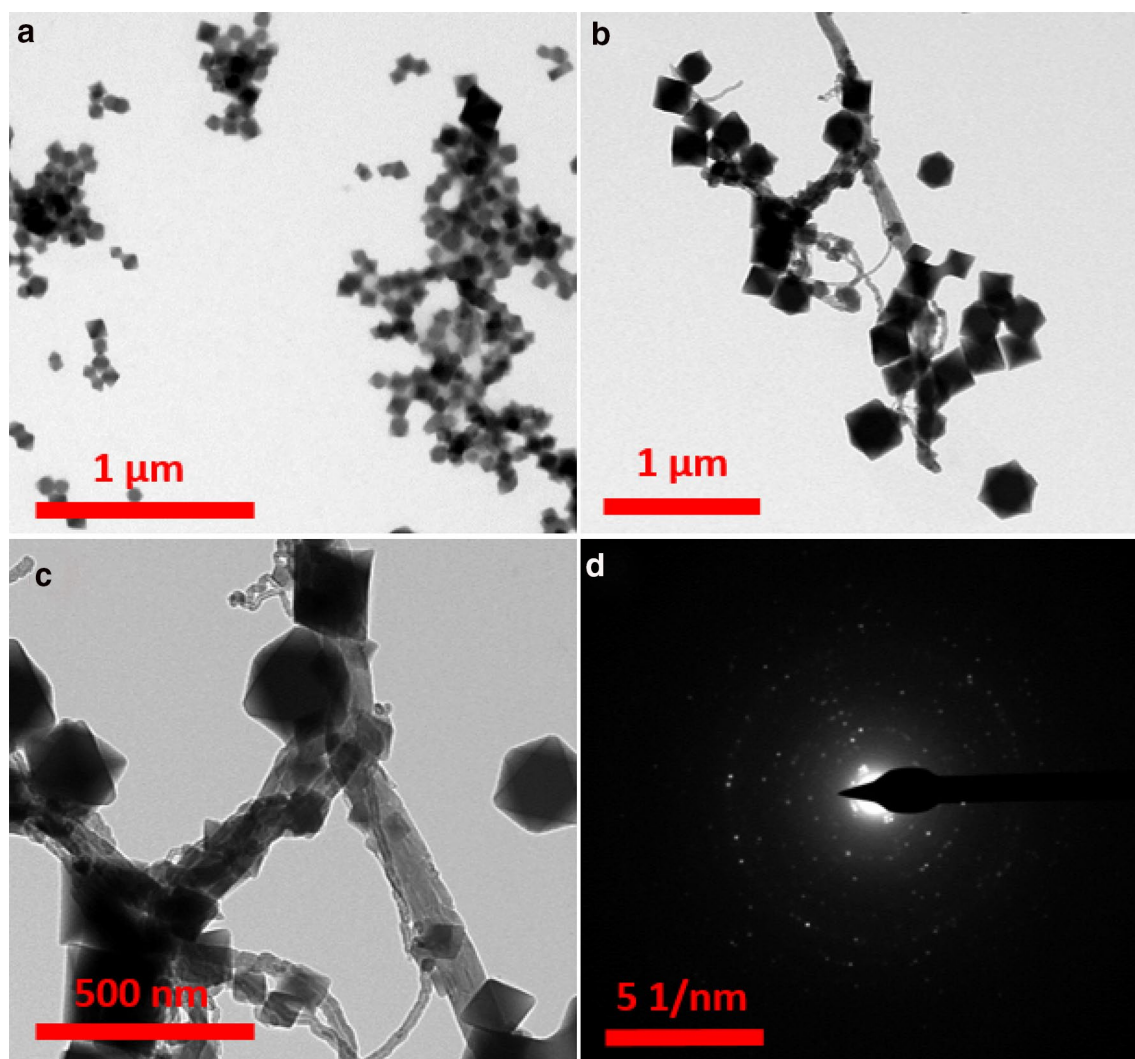
Figure 2. TEM images of (**a**) UiO-66-NH$_2$ nanoparticles, (**b**, **c**) UiO-66-NH$_2$/CNTs hybrid nanocomposite with two different magnifications, and (**d**) electron diffraction of hybrid nanocomposite.

Electrochemical studies. The EIS technique was used to study the effectiveness of synthesized nanocomposite additive on the epoxy coating life-time applied on the steel plates. Four prepared samples (See "Characterization and techniques" section) were exposed to the experimental electrolyte and EIS data were extracted in a time-dependence manner to pursue the key changes in the performance of additive-free and composite coatings over time. The electrolyte diffusion is occurred through the defects and low cross-linked regions into the organic coatings. When the electrolyte reach to the steel substrate corrosion will initiates and spreads in the coating-metal interface. So, the system degradation is inevitable at prolonged immersion times.

The Bode plots, as the most beneficial output of EIS technique, are reported in Fig. 4. The key factors in the EIS study of protective organic coatings are maximum impedance magnitude (Z_{max}), the part of Bode phase plot that is in the maximum value (θ_{-90}), number of time-constants (N_{tc}), and breakpoint frequency (f_{br}). These factors (except N_{tc}) are depicted in Fig. 5. As can be seen in Fig. 4, all samples showed one time-constant except unmodified/epoxy and UiO-66-NH$_2$/epoxy samples after 45 days. The appearance of second time-constant could be a sign of double-layer formation in the organic–inorganic interaction face[72]. The double-layer creation is due to water uptake and consequent electrolyte accumulation in some areas of the metal-coating interface. So, the corrosion process initiated in the unmodified-epoxy and UiO-66-NH$_2$/epoxy samples with longer exposures (45 days). However, the corrosion rate was not severe (See θ_{-90} description). Samples with one time-constant were in the immune region, although the corrosion rate could not be assumed to be zero. The resistance behavior observed in the bode-module plots of all samples showed that water penetrates to the metal surface through diffusion paths but the corrosion was negligible in CNTs/epoxy and composite samples due to high pore resistance values even after 45 days (See Z_{max} description). So, N_{tc} values and resistive-capacitance behavior of EIS plots confirmed that CNTs/epoxy and composite samples have relatively good corrosion resistance and two other samples were failed after 45 days.
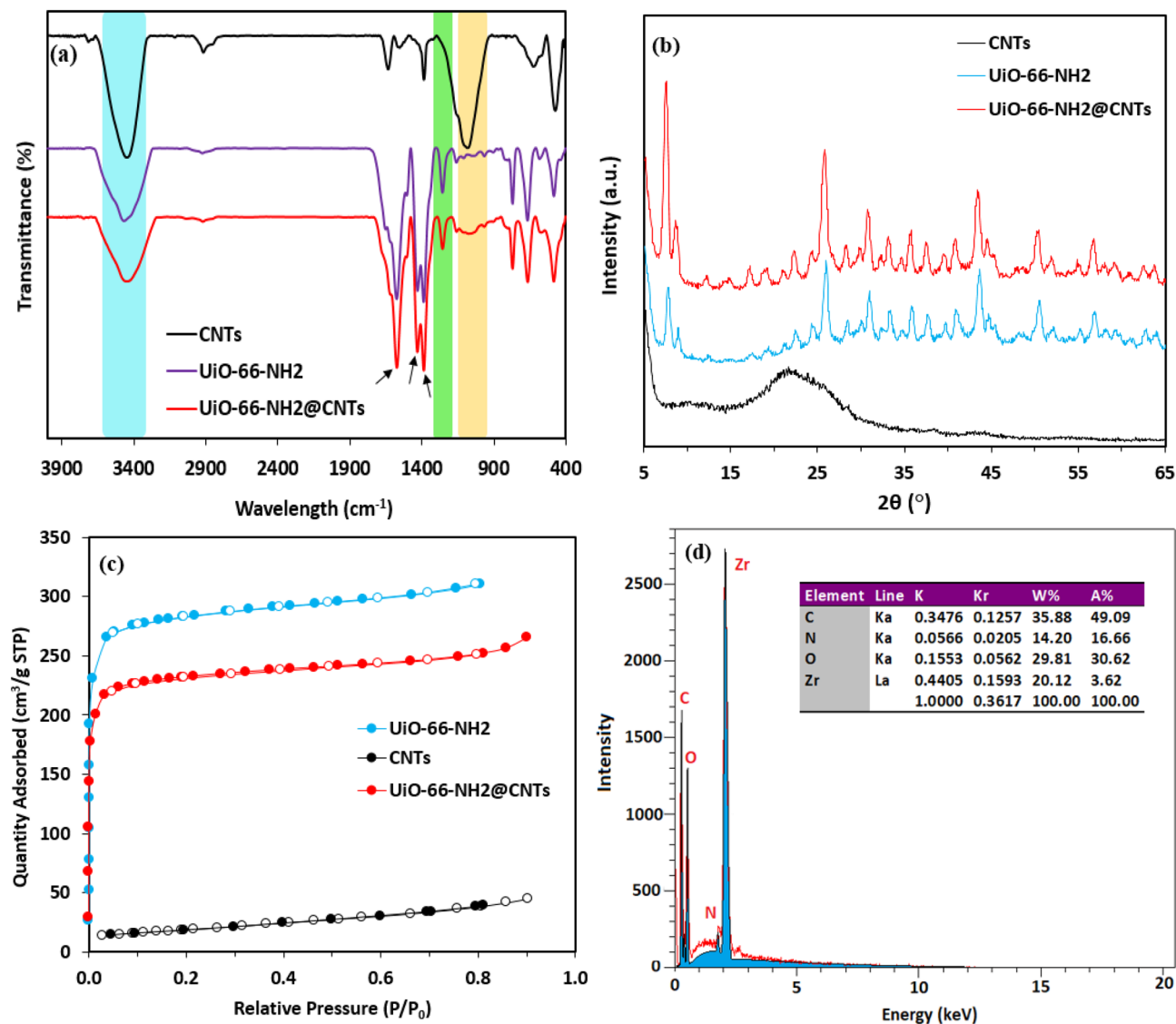
Figure 3. (**a**) FTIR analysis, (**b**) XRD patterns, and (**c**) N_2 adsorption–desorption isotherms of the prepared nanomaterials at 77 K, and (**d**) EDS analysis data of UiO-66-NH$_2$/CNTs nanocomposite.

As presented in Fig. 5a, the UiO-66-NH$_2$/CNTs/epoxy composite and UiO-66-NH$_2$/epoxy samples showed the most Z_{max} values after 15 days. Also, the Z_{max} value of UiO-66-NH$_2$/epoxy is higher than the unmodified/ epoxy and CNTs/epoxy after 15 days. The observed better performance is due to the better barrier performance of UiO-66-NH$_2$/epoxy. The UiO-66-NH$_2$ are dispersed into the coating and reinforce it against electrolyte diffusion. However, as mentioned in the introduction section, the CNTs show improper dispersion in the epoxy coating and show weaker behavior at short exposure times. However, Z_{max} followed a considerable decreasing trend for UiO-66-NH$_2$/epoxy and reduced below 6 MΩ.cm^2 after 45 days. Thus, organic–inorganic composite based on UiO-66-NH$_2$ and epoxy were not good candidates for corrosion protection of metals without any modification. The CNTs/epoxy exhibited more acceptable protective behavior related to the unmodified/epoxy and UiO-66-NH$_2$/epoxy samples at longer exposures. Although, the best performance was recorded for composite sample which Z_{max} was about 1000 MΩ.cm^2 even after 45 days[73].

According to Fig. 5b, the θ_{-90} values of unmodified/epoxy and UiO-66-NH$_2$/epoxy samples considerably decreased over time and reached close to zero after 45 days. Despite the remarkable reduction in the θ_{-90} values, the phase angle at high-frequency region still was near -90 degree, indicating that unmodified/epoxy and UiO-66-NH$_2$/epoxy were not fully destructed as per mentioned in N_{tc} description part. The recorded results for CNTs/ epoxy and composite samples were different and their ascending trend was not sharp over time. The θ_{-90} is a good criterion for estimating the activated interface area on the metal surface[74]. The higher θ_{-90} values, the lower active area. So, in accordance with the N_{tc} results, the most θ_{-90} values were observed for composite sample confirming the best performance against electrolyte penetration into the interfacial face. Finally, the f_{br} criteria was used to peruse the coating ability in contact with high saline solution over time. f_{br} is an efficient criteria to evaluate the electrochemical active area in the metal/electrolyte interface[75,76]. As observed in the Fig. 5c, the lowest log
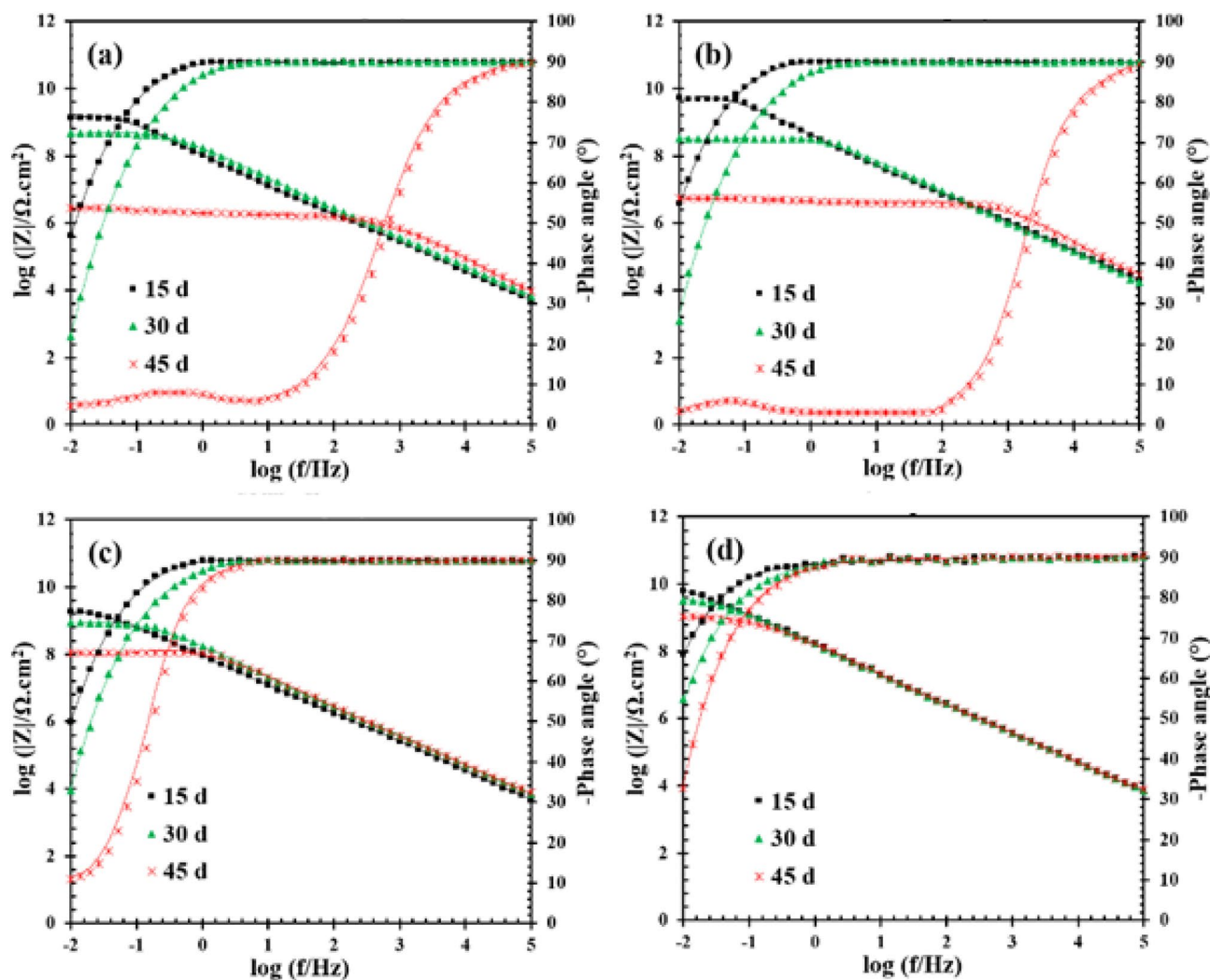
Figure 4. Bode plots of (**a**) unmodified/epoxy, (**b**) UiO-66-NH$_2$/epoxy, (**c**) CNTs/epoxy, and (**d**) composite (UiO-66-NH$_2$/CNTs/epoxy) samples after 15, 30, and 45 days at room temperature. The lines related to the fitted data.

f_{br} values were detected for composite sample at all exposure times. Also, all other samples showed positive log f_{br} values after 45 days and the worst results were obtained for unmodified/epoxy and UiO-66-NH$_2$/epoxy. According to the obtained results, the better behavior of composite sample was proved based on all experimental criteria. If reinforcement constituent in a composite form a compatible interface with the matrix material and appropriately dispersed, the resulted compact composite coating turns to a good barrier against corrosive media.

In the second part of this section, all EIS plots were fitted with appropriate equivalent circuits (ECs) and the collected data were used to better understanding the anti-corrosion behavior of composite sample. The extracted results are reported in Table 1. Also, two different ECs are illustrated in Fig. 6. The constant phase element parameter Q was used instead of ideal capacitor (C) in Fig. 6 due to the surface heterogeneity. Composite coating resistance (R_{pore}) and constant phase element parameters (Q_c and n_c) as well as double layer characteristics including charge transfer resistance (R_{ct}) and constant phase element parameters (Q_{dl} and n_{dl}) were recorded versus exposure time to find out coating-electrolyte-metal interactions. The ideal coating (C_c) and double layer (C_{dl}) capacitance were calculated as per mentioned elsewhere[77,78].

As shown in Table 1, the relative growing trend in C_c values is detected in all samples versus immersion time. Water uptake is an inevitable phenomena in organic coating exposed to the aqueous electrolytes. So, the C_c is increased by water penetration into the composite coatings. Also, the lowest C_c values were recorded for composite sample confirming the minimum water uptake among all samples. So, although the C_c could be affected by coating swelling at prolonged exposure times, it could be concluded that the barrier action of epoxy coating was reinforced by UiO-66-NH$_2$/CNTs nanocomposite additive even after relatively long exposures to high saline media[79]. However, further investigation was needed for finding the cause of lower water uptake and better corrosion protection in the composite sample. So, the hydrophobicity of the samples were studied by using of water contact angle measurement.
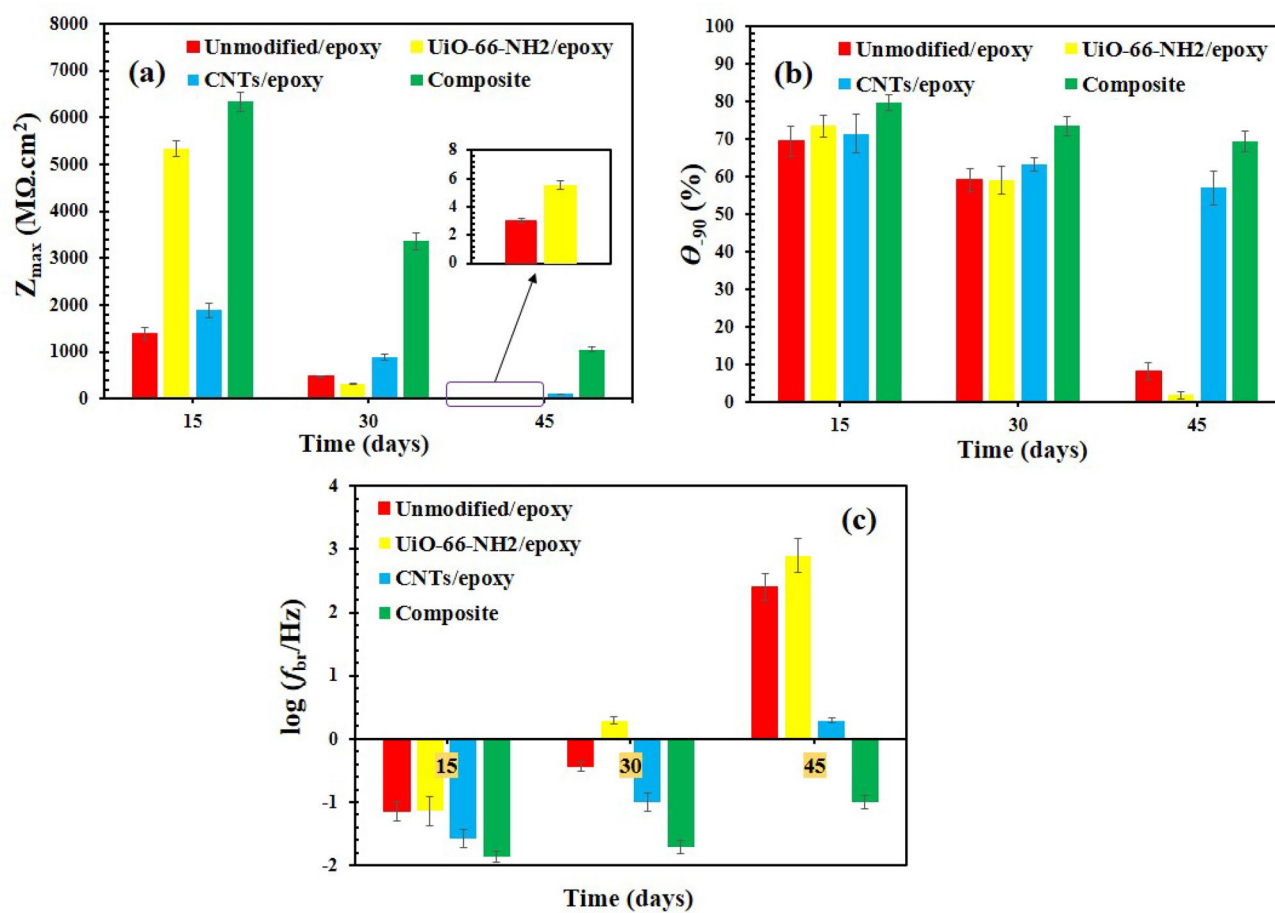
Figure 5. Extracted EIS parameters: (**a**) maximum impedance magnitude (Z_{max}), (**b**) the part of Bode phase plot that is in the maximum value (θ_{-90}), (**c**) breakpoint frequency (f_{br}) at different times: 15, 30, and 45 days (All tests have been repeated three times and the corresponding error bars are illustrated in the figures).

Sample	Time (day)	C_{dl} (µF)	R_{ct} (kΩ cm²)	C_c (nF)	R_{pore} (MΩ cm²)
Unmodified/epoxy	15	–	–	0.30	1399.6
	30	–	–	0.36	489.8
	45	22.76	651	0.53	2.8
UiO-66-NH₂/epoxy	15	–	–	0.28	5236.7
	30	–	–	0.39	325.0
	45	8.35	8832	0.57	5.5
CNTs/epoxy	15	–	–	0.29	1890.0
	30	–	–	0.31	880.1
	45	–	–	0.38	104.4
Composite (UiO-66-NH₂/CNTs/epoxy)	15	–	–	0.20	6329.6
	30	–	–	0.23	3360.0
	45	–	–	0.27	1049.2

Table 1. Fitting results of the prepared samples after different days extracted from EIS plots. (All tests have been repeated three times).

Contact angle measurement. According to Fig. 7, the lowest contact angle values are calculated on the UiO-66-NH₂ sample. In fact, the addition of UiO-66-NH₂ nanoparticles to epoxy coating results in decreasing contact angle. It could be due to the hydrophilicity nature of UiO-66-NH₂[80]. On the other hand, the composite and UiO-66-NH₂/epoxy samples show hydrophobic characteristics and a larger water contact angle[81]. So, it seems reasonable to accept that the hydrophobicity nature of composite effectively decreased the adsorption of water onto the surface; and composite and CNTs/epoxy coatings show good barrier properties in wet environments. However, the protection behavior of composite sample is considerably better than CNTs/epoxy, especially
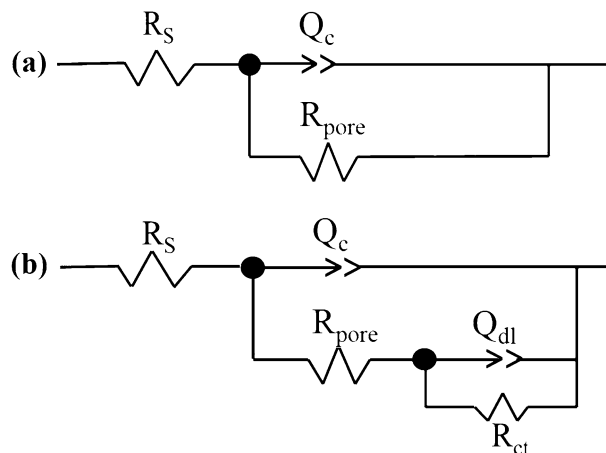
Figure 6. Equivalent circuit models with (**a**) one and (**b**) two time constants employed for analyzing the EIS results.
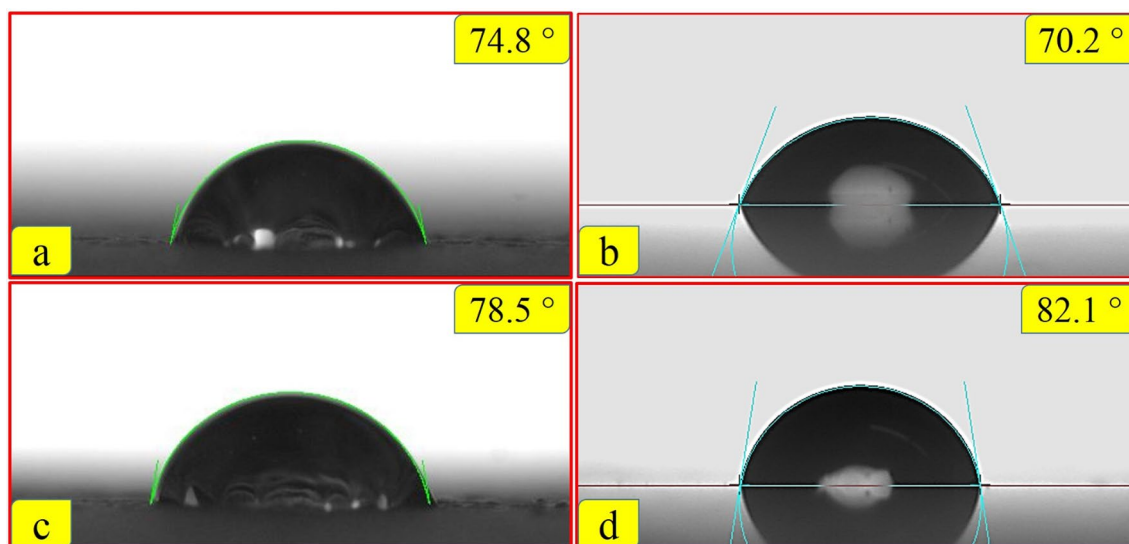

Figure 7. Contact angle measurements for the prepared coating samples: (**a**) pure epoxy, (**b**) UiO-66-NH$_2$/epoxy, (**c**) CNTs/epoxy, and (**d**) composite (UiO-66-NH$_2$/CNTs/epoxy) samples.

at longer exposures. Another factor that efficiently affects the barrier behavior of a composite coating is additive dispersion in the composite matrix. The addition of CNTs into the epoxy resin without any surface treatment is difficult due to the nanotubes aggregation[82,83]. The non-uniform dispersion of CNTs creates weak regions in the final cured epoxy system which are sensitive to wet conditions[83]. The water uptake and initiation of interfacial interactions are inevitable at prolonged exposures in the presence of these weak regions. On the other hand, UiO-66-NH$_2$/CNTs additive is appropriately dispersed in the epoxy media and yield a uniform nanocomposite coating acts as efficient barrier against wet saline environment even at long exposures.

Salt spray exposure. The salt spray test was carried out at different exposure times on the coating with artificial defect to reveal the inhibitive performance of UiO-66-NH$_2$/epoxy, CNTs/epoxy and composite samples. The visual performances of the samples are showed in Fig. 8. Corrosive media, such as chloride ions and oxygen diffuse the steel/coating interface through the micro porosities presented in the coating structure or along the scratch. When the corrosive ions penetrate the metal/coating interface, the corrosion reactions happen. So, adhesion bonds destruction and coating delamination occur due to the cathodic reactions and accumulation of corrosion product, respectively. According to Fig. 8, the corrosion reaction takes place in the scratch region of only UiO-66-NH$_2$/epoxy after 250 h. By increasing exposure time up to 500 h, corrosion process is intensified and consequent products are speared around the scratch on all samples. Also, UiO-66-NH$_2$/epoxy is the only sample shows coating delamination after 500 h. However, blisters are not appeared in all samples. Comparing the intensity of damaged area on scribe region indicates that addition of UiO-66-NH$_2$/CNTs nanocomposite to the epoxy coating caused significant decrease of the corrosion. The smaller area of corrosion damage and better visual performance of composite sample around the scratch could be attributed to the better barrier perfor-
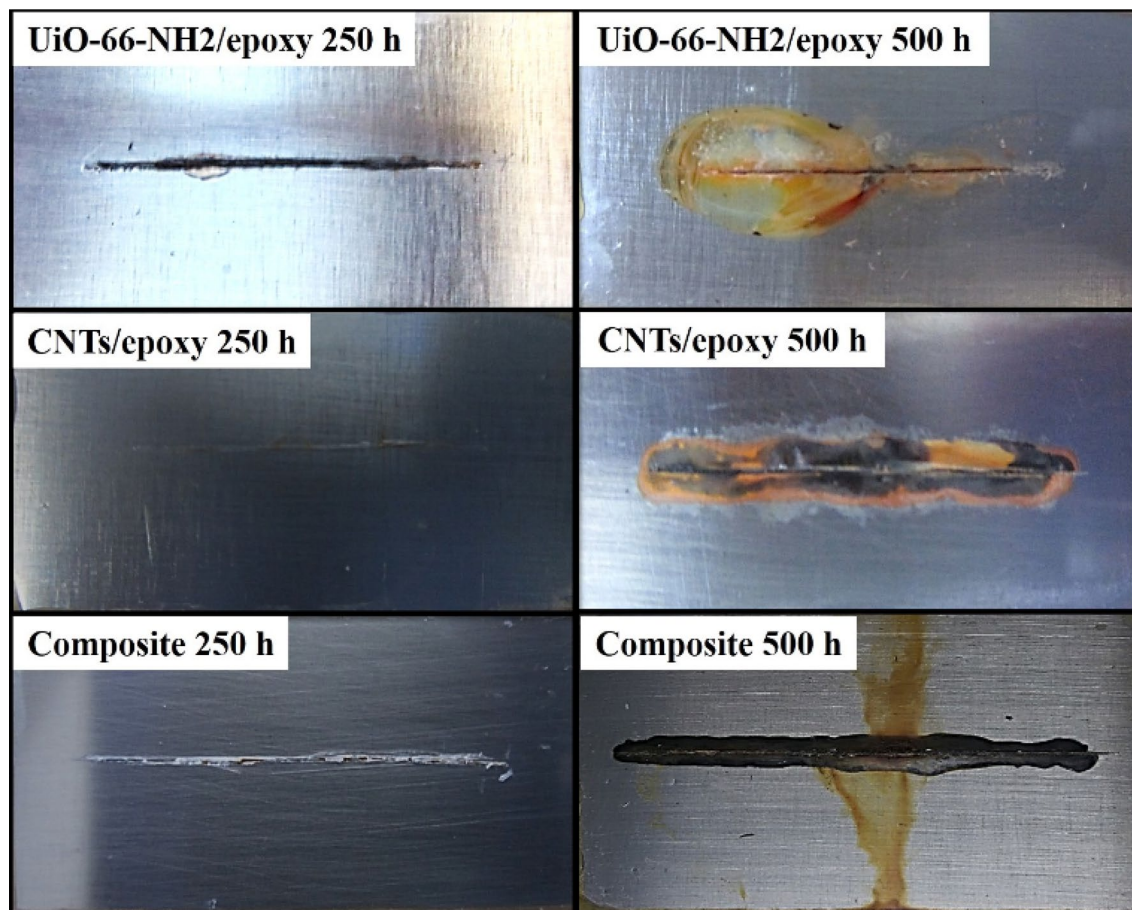
Figure 8. Visual performance of different epoxy coating samples with artificial scratch exposed to salt spray test over time.

mance against salt spray. Creation of epoxy nanocomposite coating with uniform structure and less hydrophilic nature related to non-modified epoxy coating is the key.

Protection mechanism. As presented in previous section, the protective behavior of prepared samples could be categorized into the two mechanisms. Addition of CNTs in the form of UiO-66-NH$_2$/CNTs nano-additive improve their dispersion into the epoxy matrix. So, the regions contained agglomerated additives (due to the CNTs entanglement) is not formed in the coating and the electrolyte diffusion is reduced, especially at shorter immersion times. This behavior is also observed in the UiO-66-NH$_2$/epoxy after 15 days exposure due to the relatively good dispersion of UiO-66-NH$_2$ additive. Another mechanism is based on the coating hydrophilicity. The water uptake and consequent corrosion of the substrate is proportional to the coating hydrophilic behavior. Despite acceptable anti-corrosion performance of the UiO-66-NH$_2$/epoxy at short exposure times, its protectiveness shows considerable reduction after 30 days. However, other samples show lower reduction in Z_{max} value between 15 and 30 days. On the other hand, composite sample with the most contact angle provide the best protective behavior, even after 45 days. So, it can be concluded that lower hydrophilicity and more compactness are the two reasons for better corrosion protection action of composite coating in the presence of UiO-66-NH$_2$/CNTs nano-additive.

Conclusions

Fabrication of nanocomposite coating with uniform structure and hydrophobic nature related to non-modified epoxy coating is a key solution for designing an advanced protective organic coating. Accordingly, the UiO-66-NH$_2$/CNTs nanocomposite was synthesized and epoxy-based coating was performed using this nanocomposite additive. FTIR, XRD, SEM, EDS, TEM and BET characteristic analyses were performed to confirm the synthesizing of UiO-66-NH$_2$/CNTs nanoparticles. The outcomes showed that the UiO-66-NH$_2$/CNTs nanoparticles have been successfully synthesized. The most maximum impedance magnitude (Z_{max}) and the part of Bode phase plot that is in the maximum value (θ_{-90}) and the lowest value of breakpoint frequency (f_{br}) for UiO-66-NH$_2$/CNTs/epoxy coating after long exposures in 3.5% NaCl solution indicated better performance of composite coating. The contact angle measurements represented UiO-66-NH$_2$/CNTs additive increase coating hydrophobicity related to the UiO-66-NH$_2$/epoxy and CNTs/epoxy coatings. According to the salt spray exposure, the smaller area of corrosion damage and visual performance around the scribe region confirmed that

the addition of UiO-66-NH$_2$/CNTs nanocomposite to the epoxy coating could effectively enhance corrosion properties. So, it can be concluded that the main mechanisms for better corrosion protection behavior of the composite sample are the lower coating hydrophilic nature (leading to lower water uptake) and better additives uniformity resulting in better barrier performance.

References

1. Bagherzadeh, A., Jamshidi, M. & Monemian, F. Investigating mechanical and bonding properties of micro/nano filler containing epoxy adhesives for anchoring steel bar in concrete. *Constr. Build. Mater.* **240**, 117979. https://doi.org/10.1016/j.conbuildmat.2019.117979 (2020).
2. Kameswara Reddy, M., Suresh Babu, V., Sai Srinadh, K. V. & Bhargav, M. Mechanical properties of tungsten carbide nanoparticles filled epoxy polymer nano composites. *Mater. Today Proc.* **26**, 2711–2713. https://doi.org/10.1016/j.matpr.2020.02.569 (2019).
3. Lin, Y. T. *et al.* Improvement of mechanical properties and anticorrosion performance of epoxy coatings by the introduction of polyaniline/graphene composite. *Surf. Coat. Technol.* **374**, 1128–1138. https://doi.org/10.1016/j.surfcoat.2018.01.050 (2019).
4. Novoselov, K. S. *et al.* Electric field in atomically thin carbon films. *Science (80-)* **306**, 666–669. https://doi.org/10.1126/science.1102896 (2004).
5. Hao, Y., Zhou, X., Shao, J. & Zhu, Y. The influence of multiple fillers on friction and wear behavior of epoxy composite coatings. *Surf. Coat. Technol.* **362**, 213–219. https://doi.org/10.1016/j.surfcoat.2019.01.110 (2019).
6. Cha, J., Kim, J., Ryu, S. & Hong, S. H. Comparison to mechanical properties of epoxy nanocomposites reinforced by functionalized carbon nanotubes and graphene nanoplatelets. *Compos. Part B Eng.* **162**, 283–288. https://doi.org/10.1016/j.compositesb.2018.11.011 (2019).
7. Zeng, S. *et al.* Controllable mechanical properties of epoxy composites by incorporating self-assembled carbon nanotube–montmorillonite. *Compos. Part B Eng.* **164**, 368–376. https://doi.org/10.1016/j.compositesb.2018.12.028 (2019).
8. Fang, F., Ran, S., Fang, Z., Song, P. & Wang, H. Improved flame resistance and thermo-mechanical properties of epoxy resin nanocomposites from functionalized graphene oxide via self-assembly in water. *Compos. Part B Eng.* **165**, 406–416. https://doi.org/10.1016/j.compositesb.2019.01.086 (2019).
9. Qian, Y. *et al.* Enhanced functional properties of CeO2 modified graphene/epoxy nanocomposite coating through interface engineering. *Surf. Coat. Technol.* **409**, 126819. https://doi.org/10.1016/j.surfcoat.2020.126819 (2021).
10. Li, Z., Liu, Z., Dufosse, F., Yan, L. & Wang, D. Y. Interfacial engineering of layered double hydroxide toward epoxy resin with improved fire safety and mechanical property. *Compos. Part B Eng.* **152**, 336–346. https://doi.org/10.1016/j.compositesb.2018.08.094 (2018).
11. Rafiee, M. A., Yavari, F., Rafiee, J. & Koratkar, N. Fullerene-epoxy nanocomposites-enhanced mechanical properties at low nanofiller loading. *J. Nanoparticle Res.* **13**, 733–737. https://doi.org/10.1007/s11051-010-0073-5 (2011).
12. Albdiry, M. T. & Yousif, B. F. Toughening of brittle polyester with functionalized halloysite nanocomposites. *Compos. Part B Eng.* **160**, 94–109. https://doi.org/10.1016/j.compositesb.2018.10.032 (2019).
13. Zabihi, O., Ahmadi, M., Nikafshar, S., Chandrakumar Preyeswary, K. & Naebe, M. A technical review on epoxy-clay nanocomposites: Structure, properties, and their applications in fiber reinforced composites. *Compos. Part B Eng.* **135**, 1–24. https://doi.org/10.1016/j.compositesb.2017.09.066 (2018).
14. Wang, Q. & Astruc, D. State of the art and prospects in metal–organic framework (MOF)-based and MOF-derived nanocatalysis. *Chem. Rev.* **120**, 1438–1511. https://doi.org/10.1021/acs.chemrev.9b00223 (2020).
15. Abdi, J. & Abedini, H. MOF-based polymeric nanocomposite beads as an efficient adsorbent for wastewater treatment in batch and continuous systems: Modelling and experiment. *Chem. Eng. J.* **400**, 125862. https://doi.org/10.1016/j.cej.2020.125862 (2020).
16. Abdi, J., Vossoughi, M., Mahmoodi, N. M. & Alemzadeh, I. Synthesis of metal–organic framework hybrid nanocomposites based on GO and CNT with high adsorption capacity for dye removal. *Chem. Eng. J.* **326**, 1145–1158. https://doi.org/10.1016/j.cej.2017.06.054 (2017).
17. Abdi, J., Banisharif, F. & Khataee, A. Amine-functionalized Zr-MOF/CNTs nanocomposite as an efficient and reusable photocatalyst for removing organic contaminants. *J. Mol. Liq.* **334**, 116129. https://doi.org/10.1016/j.molliq.2021.116129 (2021).
18. Abdi, J. Synthesis of Ag-doped ZIF-8 photocatalyst with excellent performance for dye degradation and antibacterial activity. *Colloids Surf. A Physicochem. Eng. Asp.* **604**, 125330. https://doi.org/10.1016/j.colsurfa.2020.125330 (2020).
19. Zhu, J. *et al.* Facile preparation of superhydrophobic metal meshes with micro-hierarchical structure via in situ self-assembly metal–organic framework for efficient oil–water separation. *Surf. Coat. Technol.* **402**, 126344. https://doi.org/10.1016/j.surfcoat.2020.126344 (2020).
20. Wu, C. *et al.* Fabrication of ZIF-8@SiO2 micro/nano hierarchical superhydrophobic surface on AZ31 magnesium alloy with impressive corrosion resistance and abrasion resistance. *ACS Appl. Mater. Interfaces.* **9**, 11106–11115. https://doi.org/10.1021/acsami.6b16848 (2017).
21. Guo, Y., Wang, J., Zhang, D., Qi, T. & Li, G. L. pH-responsive self-healing anticorrosion coatings based on benzotriazole-containing zeolitic imidazole framework. *Colloids Surf. A Physicochem. Eng. Asp.* **561**, 1–8. https://doi.org/10.1016/j.colsurfa.2018.10.044 (2019).
22. Liu, W. *et al.* Mg-MOF-74/MgF2 composite coating for improving the properties of magnesium alloy implants: Hydrophilicity and corrosion resistance. *Materials (Basel).* **11**, 1–9. https://doi.org/10.3390/ma11030396 (2018).
23. Etaiw, S. E. H., Fouda, A. E. A. S., Abdou, S. N. & El-bendary, M. M. Structure, characterization and inhibition activity of new metal–organic framework. *Corros. Sci.* **53**, 3657–3665. https://doi.org/10.1016/j.corsci.2011.07.007 (2011).
24. Zafari, S., Niknam Shahrak, M. & Ghahramaninezhad, M. New MOF-based corrosion inhibitor for carbon steel in acidic media. *Met. Mater. Int.* **26**, 25–38. https://doi.org/10.1007/s12540-019-00307-1 (2020).
25. Cao, K., Yu, Z. & Yin, D. Preparation of Ce-MOF@TEOS to enhance the anti-corrosion properties of epoxy coatings. *Prog. Org. Coat.* **135**, 613–621. https://doi.org/10.1016/j.porgcoat.2019.06.015 (2019).
26. Lashgari, S. M. *et al.* Application of nanoporous cobalt-based ZIF-67 metal–organic framework (MOF) for construction of an epoxy-composite coating with superior anti-corrosion properties. *Corros. Sci.* **178**, 109099. https://doi.org/10.1016/j.corsci.2020.109099 (2021).
27. Zhang, M., Ma, L., Wang, L., Sun, Y. & Liu, Y. Insights into the use of metal–organic framework as high-performance anticorrosion coatings. *ACS Appl. Mater. Interfaces.* **10**, 2259–2263. https://doi.org/10.1021/acsami.7b18713 (2018).
28. Tian, H. *et al.* Controlled delivery of multi-substituted triazole by metal–organic framework for efficient inhibition of mild steel corrosion in neutral chloride solution. *Corros. Sci.* **131**, 1–16. https://doi.org/10.1016/j.corsci.2017.11.010 (2018).
29. Kumaraguru, S., Pavulraj, R. & Mohan, S. Influence of cobalt, nickel and copper-based metal–organic frameworks on the corrosion protection of mild steel. *Trans. Inst. Met. Finish.* **95**, 131–136. https://doi.org/10.1080/00202967.2017.1283898 (2017).

30. Fouda, A. E. A. S., Etaiw, S. E. D. H., El-Bendary, M. M. & Maher, M. M. Metal–organic frameworks based on silver (I) and nitrogen donors as new corrosion inhibitors for copper in HCl solution. *J. Mol. Liq.* **213**, 228–234. https://doi.org/10.1016/j.molliq.2015.11.001 (2016).

31. Zheng, Q. *et al.* Metal–organic frameworks incorporated polycaprolactone film for enhanced corrosion resistance and biocompatibility of Mg alloy. *ACS Sustain. Chem. Eng.* **7**, 18114–18124. https://doi.org/10.1021/acssuschemeng.9b05196 (2019).

32. Roy, S., Suresh, V. M. & Maji, T. K. Self-cleaning MOF: Realization of extreme water repellence in coordination driven self-assembled nanostructures. *Chem. Sci.* **7**, 2251–2256. https://doi.org/10.1039/c5sc03676c (2016).

33. Etaiw, S. E. H., Fouda, A. E. A. S., Amer, S. A. & El-bendary, M. M. Structure, characterization and anti-corrosion activity of the new metal–organic framework [Ag(qox)(4-ab)]. *J. Inorg. Organomet. Polym. Mater.* **21**, 327–335. https://doi.org/10.1007/s10904-011-9467-9 (2011).

34. Kalmutzki, M. J., Hanikel, N. & Yaghi, O. M. Secondary building units as the turning point in the development of the reticular chemistry of MOFs. *Sci. Adv.* https://doi.org/10.1126/sciadv.aat9180 (2018).

35. Abdi, J., Vossoughi, M., Mahmoodi, N. M. & Alemzadeh, I. Synthesis of amine-modified zeolitic imidazolate framework-8, ultrasound-assisted dye removal and modeling. *Ultrason. Sonochem.* **39**, 550–564. https://doi.org/10.1016/j.ultsonch.2017.04.030 (2017).

36. Zhang, X. *et al.* Enhanced adsorption performance of gaseous toluene on defective UiO-66 metal organic framework: Equilibrium and kinetic studies. *J. Hazard. Mater.* **365**, 597–605. https://doi.org/10.1016/j.jhazmat.2018.11.049 (2019).

37. Zhang, X., Lv, X., Shi, X., Yang, Y. & Yang, Y. Enhanced hydrophobic UiO-66 (University of Oslo 66) metal–organic framework with high capacity and selectivity for toluene capture from high humid air. *J. Colloid Interface Sci.* **539**, 152–160. https://doi.org/10.1016/j.jcis.2018.12.056 (2019).

38. Burtch, N. C., Jasuja, H. & Walton, K. S. Water stability and adsorption in metal–organic frameworks. *Chem. Rev.* **114**, 10575–10612. https://doi.org/10.1021/cr5002589 (2014).

39. Yang, D. & Gates, B. C. Catalysis by metal organic frameworks: Perspective and suggestions for future research. *ACS Catal.* **9**, 1779–1798. https://doi.org/10.1021/acscatal.8b04515 (2019).

40. Zhang, X., Lv, X., Bi, F., Lu, G. & Wang, Y. Highly efficient Mn2O3 catalysts derived from Mn-MOFs for toluene oxidation: The influence of MOFs precursors. *Mol. Catal.* **482**, 110701. https://doi.org/10.1016/j.mcat.2019.110701 (2020).

41. Dhakshinamoorthy, A., Li, Z. & Garcia, H. Catalysis and photocatalysis by metal organic frameworks. *Chem. Soc. Rev.* **47**, 8134–8172. https://doi.org/10.1039/c8cs00256h (2018).

42. Dhakshinamoorthy, A., Santiago-Portillo, A., Asiri, A. M. & Garcia, H. Engineering UiO-66 metal organic framework for heterogeneous catalysis. *ChemCatChem* **11**, 899–923. https://doi.org/10.1002/cctc.201801452 (2019).

43. Freund, R. *et al.* The current status of MOF and COF applications. *Angew. Chem. Int. Ed.* **60**, 23975–24001. https://doi.org/10.1002/anie.202106259 (2021).

44. Xiao, J. D. & Jiang, H. L. Metal–organic frameworks for photocatalysis and photothermal catalysis. *Acc. Chem. Res.* https://doi.org/10.1021/acs.accounts.8b00521 (2018).

45. Abdi, J., Yahyanezhad, M., Sakhaie, S., Vossoughi, M. & Alemzadeh, I. Synthesis of porous TiO2/ZrO2 photocatalyst derived from zirconium metal organic framework for degradation of organic pollutants under visible light irradiation. *J. Environ. Chem. Eng.* **7**, 103096. https://doi.org/10.1016/j.jece.2019.103096 (2019).

46. Zhang, X. *et al.* Catalytic oxidation of toluene using a facile synthesized Ag nanoparticle supported on UiO-66 derivative. *J. Colloid Interface Sci.* **571**, 38–47. https://doi.org/10.1016/j.jcis.2020.03.031 (2020).

47. Mahmoodi, N. M. & Abdi, J. Nanoporous metal–organic framework (MOF-199): Synthesis, characterization and photocatalytic degradation of Basic Blue 41. *Microchem. J.* **144**, 436–442. https://doi.org/10.1016/j.microc.2018.09.033 (2019).

48. Zhang, J., Li, Z., Qi, X., Zhang, W. & Wang, D. Y. Size tailored bimetallic metal–organic framework (MOF) on graphene oxide with sandwich-like structure as functional nano-hybrids for improving fire safety of epoxy. *Compos. Part B Eng.* **188**, 107881. https://doi.org/10.1016/j.compositesb.2020.107881 (2020).

49. Guo, W. *et al.* Construction of SiO2@UiO-66 core–shell microarchitectures through covalent linkage as flame retardant and smoke suppressant for epoxy resins. *Compos. Part B Eng.* **176**, 107261. https://doi.org/10.1016/j.compositesb.2019.107261 (2019).

50. Ramezanzadeh, M., Ramezanzadeh, B., Mahdavian, M. & Bahlakeh, G. Development of metal–organic framework (MOF) decorated graphene oxide nanoplatforms for anti-corrosion epoxy coatings. *Carbon N. Y.* **161**, 231–251. https://doi.org/10.1016/j.carbon.2020.01.082 (2020).

51. Motamedi, M., Ramezanzadeh, M., Ramezanzadeh, B. & Mahdavian, M. One-pot synthesis and construction of a high performance metal–organic structured nano pigment based on nanoceria decorated cerium (III)-imidazole network (NC/CIN) for effective epoxy composite coating anti-corrosion and thermo-mechanical properties impro. *Chem. Eng. J.* **382**, 122820. https://doi.org/10.1016/j.cej.2019.122820 (2020).

52. Ma, S. *et al.* Metal–organic framework@polyaniline nanoarchitecture for improved fire safety and mechanical performance of epoxy resin. *Mater. Chem. Phys.* **247**, 122875. https://doi.org/10.1016/j.matchemphys.2020.122875 (2020).

53. Zhang, J., Li, Z., Zhang, L., García Molleja, J. & Wang, D. Y. Bimetallic metal–organic framework and graphene oxide nano-hybrids induced carbonaceous reinforcement towards fire retardant epoxy: A novel alternative carbonization mechanism. *Carbon N. Y.* **153**, 407–416. https://doi.org/10.1016/j.carbon.2019.07.003 (2019).

54. Cavka, J. H. *et al.* A new zirconium inorganic building brick forming metal organic frameworks with exceptional stability. *J. Am. Chem. Soc.* **130**, 13850–13851. https://doi.org/10.1021/ja8057953 (2008).

55. Vermoortele, F., Vimont, A., Serre, C. & De Vos, D. An amino-modified Zr-terephthalate metal–organic framework as an acid–base catalyst for cross-aldol condensation. *Chem. Commun.* **47**, 1521–1523. https://doi.org/10.1039/c0cc03038d (2011).

56. Ramezanzadeh, M., Tati, A., Bahlakeh, G. & Ramezanzadeh, B. Construction of an epoxy composite coating with exceptional thermo-mechanical properties using Zr-based NH2-UiO-66 metal–organic framework (MOF): Experimental and DFT-D theoretical explorations. *Chem. Eng. J.* **408**, 127366. https://doi.org/10.1016/j.cej.2020.127366 (2021).

57. Kandiah, M. *et al.* Synthesis and stability of tagged UiO-66 Zr-MOFs. *Chem. Mater.* **22**, 6632–6640. https://doi.org/10.1021/cm102601v (2010).

58. Nazari, M. *et al.* Metal–organic-framework-coated optical fibers as light-triggered drug delivery vehicles. *Adv. Funct. Mater.* **26**, 3244–3249. https://doi.org/10.1002/adfm.201505260 (2016).

59. Bai, Y. *et al.* Zr-based metal–organic frameworks: Design, synthesis, structure, and applications. *Chem. Soc. Rev.* **45**, 2327–2367. https://doi.org/10.1039/c5cs00837a (2016).

60. Sai, T., Ran, S., Guo, Z. & Fang, Z. A Zr-based metal organic frameworks towards improving fire safety and thermal stability of polycarbonate. *Compos. Part B Eng.* **176**, 107198. https://doi.org/10.1016/j.compositesb.2019.107198 (2019).

61. Sharma, V. *et al.* Recent progress in nano-oxides and CNTs based corrosion resistant superhydrophobic coatings: A critical review. *Prog. Org. Coat.* **140**, 105512. https://doi.org/10.1016/j.porgcoat.2019.105512 (2020).

62. Zeng, Z. *et al.* Heterogeneous growth of UiO-66-NH2on oxidized single-walled carbon nanotubes to form "beads-on-a-string" composites. *ACS Appl. Mater. Interfaces.* **13**, 15482–15489. https://doi.org/10.1021/acsami.0c21509 (2021).

63. Sang, X. *et al.* Interfacial growth of metal–organic framework on carboxyl-functionalized carbon nanotubes for efficient dye adsorption and separation. *Anal. Methods.* **12**, 4534–4540. https://doi.org/10.1039/d0ay01490a (2020).

64. Sun, X. *et al.* Preparation of a chemically stable metal–organic framework and multi-walled carbon nanotube composite as a high-performance electrocatalyst for the detection of lead. *Analyst.* **145**, 1833–1840. https://doi.org/10.1039/c9an02299f (2020).

65. Li, Y. *et al.* A UiO-66-NH2/carbon nanotube nanocomposite for simultaneous sensing of dopamine and acetaminophen. *Anal. Chim. Acta.* **1158**, 338419. https://doi.org/10.1016/j.aca.2021.338419 (2021).

66. Wang, X. *et al.* Fabrication of heterostructured UIO-66-NH2 /CNTs with enhanced activity and selectivity over photocatalytic CO2 reduction. *Int. J. Hydrog. Energy.* **45**, 30634–30646. https://doi.org/10.1016/j.ijhydene.2020.08.273 (2020).

67. Zhang, X., Zhang, Y., Wang, T., Fan, Z. & Zhang, G. A thin film nanocomposite membrane with pre-immobilized UiO-66-NH2 toward enhanced nanofiltration performance. *RSC Adv.* **9**, 24802–24810. https://doi.org/10.1039/c9ra04714j (2019).

68. Sun, J., Feng, S. & Feng, S. Hydrothermally synthesis of MWCNT/N-TiO2/UiO-66-NH2 ternary composite with enhanced photo-catalytic performance for ketoprofen. *Inorg. Chem. Commun.* **111**, 107669. https://doi.org/10.1016/j.inoche.2019.107669 (2020).

69. Zhao, W. *et al.* Decorating Ag/AgCl on UiO-66-NH2: Synergy between Ag plasmons and heterostructure for the realization of efficient visible light photocatalysis, Chinese. *J. Catal.* **40**, 1187–1197. https://doi.org/10.1016/S1872-2067(19)63377-2 (2019).

70. Cao, A., Xu, C., Liang, J., Wu, D. & Wei, B. X-ray diffraction characterization on the alignment degree of carbon nanotubes. *Chem. Phys. Lett.* **344**, 13–17. https://doi.org/10.1016/S0009-2614(01)00671-6 (2001).

71. Wang, L., Zheng, P., Zhou, X., Xu, M. & Liu, X. Facile fabrication of CdS/UiO-66-NH 2 heterojunction photocatalysts for efficient and stable photodegradation of pollution. *J. Photochem. Photobiol. A Chem.* **376**, 80–87. https://doi.org/10.1016/j.jphotochem.2019.03.001 (2019).

72. Mohammadi, I., Shahrabi, T., Mahdavian, M. & Izadi, M. Improving the protection performance of AA2024-T3 in 3.5 wt% NaCl solution using the synergistic effect of cerium cations and diethyldithiocarbamate molecules. *J. Electrochem. Soc.* **167**, 131506. https://doi.org/10.1149/1945-7111/abb70e (2020).

73. Izadi, M., Yazdiyan, A., Shahrabi, T., Hoseinieh, S. M. & Shahrabi, H. Influence of temperature variation on the formation and cor-rosion protective performance of calcium carbonate deposits in artificial seawater. *J. Mater. Eng. Perform.* **28**, 4221–4233. https://doi.org/10.1007/s11665-019-04189-7 (2019).

74. Ramezanzadeh, B., Ghasemi, E., Askari, F. & Mahdavian, M. Synthesis and characterization of a new generation of inhibitive pig-ment based on zinc acetate/benzotriazole: Solution phase and coating phase studies. *Dyes Pigment* **122**, 331–345. https://doi.org/10.1016/j.dyepig.2015.07.013 (2015).

75. Rostami, M., Rasouli, S., Ramezanzadeh, B. & Askari, A. Electrochemical investigation of the properties of Co doped ZnO nano-particle as a corrosion inhibitive pigment for modifying corrosion resistance of the epoxy coating. *Corros. Sci.* **88**, 387–399. https://doi.org/10.1016/j.corsci.2014.07.056 (2014).

76. Feng, Z. & Frankel, G. S. Evaluation of coated Al alloy using the breakpoint frequency method. *Electrochim. Acta* **187**, 605–615. https://doi.org/10.1016/j.electacta.2015.11.114 (2016).

77. Izadi, M., Rad, A. R., Shahrabi, T. & Mohammadi, I. The combined action of L-cysteine and L-histidine as a significant eco-friendly protective system to enhance the corrosion protection performance of AA2024-T3 alloy in 0.1 M NaCl solution: Electrochemical and surface studies. *Mater. Chem. Phys.* **250**, 122997. https://doi.org/10.1016/j.matchemphys.2020.122997 (2020).

78. Mohammadi, I., Shahrabi, T., Mahdavian, M. & Izadi, M. Sodium diethyldithiocarbamate as a novel corrosion inhibitor to mitigate corrosion of 2024–T3 aluminum alloy in 3.5 wt% NaCl solution. *J. Mol. Liq.* **307**, 112965. https://doi.org/10.1016/j.molliq.2020.112965 (2020).

79. Stimpfling, T., Leroux, F. & Hintze-Bruening, H. Unraveling EDTA corrosion inhibition when interleaved into Layered Double Hydroxide epoxy filler system coated onto aluminum AA 2024. *Appl. Clay Sci.* **83–84**, 32–41. https://doi.org/10.1016/j.clay.2013.08.005 (2013).

80. Zhang, F. *et al.* Converting metal–organic framework particles from hydrophilic to hydrophobic by an interfacial assembling route. *Langmuir* **33**, 12427–12433. https://doi.org/10.1021/acs.langmuir.7b02365 (2017).

81. Yum, S. G., Yin, H. & Jang, S. H. Toward multi-functional road surface design with the nanocomposite coating of carbon nanotube modified polyurethane: Lab-scale experiments. *Nanomaterials* **10**, 1–7. https://doi.org/10.3390/nano10101905 (2020).

82. Deyab, M. A. & Awadallah, A. E. Advanced anticorrosive coatings based on epoxy/functionalized multiwall carbon nanotubes composites. *Prog. Org. Coat.* **139**, 105423. https://doi.org/10.1016/j.porgcoat.2019.105423 (2020).

83. Ma, P. C., Mo, S. Y., Tang, B. Z. & Kim, J. K. Dispersion, interfacial interaction and re-agglomeration of functionalized carbon nanotubes in epoxy composites. *Carbon N. Y.* **48**, 1824–1834. https://doi.org/10.1016/j.carbon.2010.01.028 (2010).

Acknowledgements

Author contributions

J.A. and M.B. designed the study, J.A. synthesized and characterized the prepared nano-materials and the elec-trochemical measurements were performed by M.I. and M.B. All authors discussed the results and contributed to the final manuscript.

Competing interests

The authors declare no competing interests.

Additional information

Supplementary Information The online version contains supplementary material available at https://doi.org/10.1038/s41598-022-14854-y.

Correspondence and requests for materials should be addressed to M.B.

Reprints and permissions information is available at www.nature.com/reprints.

Publisher's note Springer Nature remains neutral with regard to jurisdictional claims in published maps and institutional affiliations.